A Compact Fabry-Perot Interferometer with a Solid Etalon for Measuring Upper Atmospheric Wind and Temperature

Tiancai Wang[1,3], **Yajun Zhu**[1,2,3], **Guangyi Zhu**[1,3], **Wei Yuan**[1,3], **Zhongqi Tan**[4], **Weijun Liu**[1,3], **Qiucheng Gong**[4], **Hong Gao**[1,2,3], **and Jiyao Xu**[1,2,3]

[1]State Key Laboratory of Solar Activity and Space Weather, National Space Science Center, Chinese Academy of Sciences, Beijing, 100190, China
[2]University of Chinese Academy of Sciences, Beijing, 100049, China
[3] National Field Observation and Research Station (Hainan) for Space Weather, Hainan, 571734, China
[4] College of Advanced Interdisciplinary Studies, National University of Defense Technology, Changsha, 410073, China

Correspondence: Yajun Zhu (y.zhu@swl.ac.cn) and Qiucheng Gong (gong.qiucheng@nudt.edu.cn)

Abstract. A compact solid-etalon Fabry-Perot interferometer (SEFPI) with a 70 mm-diameter solid fused-silica etalon has been developed for ground-based measurements of upper atmospheric winds and temperatures at an altitude of approximately 250 km. Unlike conventional FPIs employing air-spaced etalons, the SEFPI uses a solid etalon, enabling a more compact, lightweight, and cost-effective instrument design, while requiring stringent thermal stabilization. Laboratory validation using an acousto-optic frequency shifter (AOFS) to generate controlled Doppler shifts demonstrated the SEFPI's high measurement accuracy, with an average wind uncertainty of 0.42 m/s and a root mean square error (RMSE) of 0.61 m/s. Preliminary field validation and intercomparisons were conducted via coincident ground-based measurements with two interferometry techniques. The first employed a Dual-Channel Optical Interferometer (DCOI), while the second used a well-established FPI employing a 100 mm-diameter air-spaced etalon. The SEFPI measurements exhibited strong agreement with both instruments, yielding Pearson correlation coefficients exceeding 0.84. Statistical analysis yielded a mean difference (DCOI/FPI - SEFPI), averaged across both meridional and zonal wind components, of +1.88 m/s relative to the co-located DCOI instrument and +5.58 m/s relative to the conventional FPI located 502 km away. Temperature comparisons between the two FPIs revealed a correlation coefficient of 0.86, with a mean difference (FPI - SEFPI) of +62.38 K.

1 Introduction

The Earth's upper atmosphere serves as a key transition region from the lower atmosphere to outer space and is highly dynamic. This region is dominated by a combination of in situ forcing, driven by the absorption of solar extreme ultraviolet (EUV) radiation, and upward-propagating atmospheric disturbances such as tides, gravity waves, and planetary waves, originating in the lower atmosphere (Fisher et al., 2002). Neutral winds and temperatures play a critical role in determining the state, evolution, and dynamics of the global Ionosphere-Thermosphere system. Furthermore, dynamical changes in neutral winds directly or indirectly perturb the ionosphere, thereby giving rise to electric fields and plasma instabilities. These phenomena, in turn, affect the global redistribution of energy and momentum deposited at high latitudes by the magnetosphere (Dhadly et al., 2023; Makela et al., 2014, 2021). Despite their recognized significance, neutral winds and temperatures remain among the least comprehensively sampled state parameters within the global upper atmosphere even after decades of observations. Accurate measurements of upper atmospheric winds and temperatures are therefore essential for advancing our understanding of these coupled processes. This endeavor advances our understanding of the complexities of the Earth's atmosphere, as well as our ability to predict the effects of solar and geomagnetic activity, atmospheric perturbations, and other phenomena on the Earth's environment and technological systems (Immel et al., 2021; Li et al., 2023; Liu et al., 2015; Oyama et al., 2024; Yang et al., 2020).

One of the most effective methods for measuring neutral winds and temperatures, particularly in the upper atmosphere, is through airglow observations using interferometric spectroscopy. Airglow, an important tracer of variability in the middle and

upper atmosphere, is produced by atmospheric photochemical processes (Gao et al., 2011; Saha and Pallamraju, 2022). Photons emitted during these processes enable passive optical remote sensing of winds and temperatures. Among passive optical techniques, the Fabry-Perot interferometer (FPI) has remained one of the most widely used instruments for nocturnal measurements of neutral winds and temperatures (Dhadly et al., 2023; Englert et al., 2010; Grawe et al., 2019; Meriwether, 2006; Okoh et al., 2022; Wu et al., 2019). It operates by monitoring Doppler shifts and spectral broadening in selected nightglow emissions. While radars, lidars, and ionosondes provide valuable data on atmospheric parameters at various altitudes, passive optical interferometry remains one of the few ground-based techniques capable of directly measuring atmospheric winds at altitudes around 250 km (Dao et al., 1995; Englert et al., 2012; Jia et al., 2025; Kristoffersen et al., 2024; Li et al., 2025; Sun et al., 2024; Tsuda, 2014; Yi et al., 2019; Yue et al., 2022; Zhang et al., 2025).

Over the past few decades, various types of FPIs have been developed to meet the increasing demand for accurate wind and temperature measurements relevant to space environment monitoring. Based on their optical configuration and field of view (FoV), FPIs can generally be categorized as all-sky and single-point measurement systems. All-sky FPIs use a fore-optics assembly that includes a fisheye lens to achieve a wide FoV, enabling simultaneous measurements of wind and temperature over a large region of the sky, providing high temporal and spatial resolution (Anderson et al., 2009; Aruliah et al., 2010; Biondi et al., 1995; Conde and Smith, 1997; Shiokawa et al., 2001). In contrast, single-point FPIs with a narrow FoV possess simpler optical configurations. For wind and temperature measurements, single-point FPIs require a sky scanner equipped with a dual-axis mirror to steer the system, directing light from any region of the sky into the system aperture (Makela et al., 2009; Meriwether et al., 1983; Shiokawa et al., 2012; Trondsen et al., 2019; Vasilyev et al., 2017; Wu et al., 2004). A complete measurement cycle usually includes observations at the zenith and at 45° elevation in the four cardinal directions (east, south, west, and north) and is typically followed by laser calibration. To date, virtually all existing FPI systems employ air-spaced etalons enclosed in metal housings to ensure thermal and mechanical stability (Hernandez, 1980; Meriwether, 2006; Nakajima et al., 1995; Vasilyev et al., 2017; Wang et al., 2025; Wu et al., 2004). To increase the signal-to-noise ratio (SNR) for observing faint nightglow, FPIs generally utilize large-aperture etalons, often with diameters of at least 100 mm (Anderson et al., 2009; Jacka et al., 1980; Schmidt et al., 2025; Sivjee et al., 1980; Wang et al., 2016). However, such etalons are typically heavy and expensive, as fabrication complexity increases exponentially with aperture size. As a result, the establishment of large-scale ground-based FPI observational networks has been hindered by the bulky and expensive nature of these instruments.

To address these limitations and advance ground-based passive optical observational networks for middle- and upper-atmospheric measurements, a novel solid-etalon Fabry-Perot interferometer (SEFPI) has been developed and validated through laboratory experiments and field observations. For applications where instrument size and weight are constrained, the SEFPI system built from a solid etalon is an interesting option to explore, as it is compact, pressure-insensitive and low-cost, and provides an alternative to customized air-spaced etalons. The paper is organized as follows: Section 2 details the optical design of the SEFPI. In Section 3, the instrument function of the FPI is adapted for the solid etalon, and a forward model for retrieving wind and temperature is derived. Section 4 demonstrates SEFPI's robust wind measurement capabilities using newly developed high-accuracy laboratory setups for simulating wind speed. Section 5 presents SEFPI's initial wind and temperature measurements at an altitude of 250 km and validates them by cross-comparing them with data from two independent ground-based passive optical instruments deployed at two sites. Finally, Section 6 summarizes and discusses the findings of this study.

2 Instrumentation

The SEFPI's optical configuration and a photograph of the instrument deployed at the observation station are shown in Figure 1, with detailed descriptions and specifications of each component provided in Table 1. A key component of the system is the sky scanner, which is equipped with a pair of dual-axis steering mirrors. These mirrors can be independently rotated to select the desired azimuth and zenith angles, directing light from any region of the sky into the SEFPI aperture. The sky scanner is

mechanically isolated from the main SEFPI body and mounted separately above it to minimize mechanical vibrations and associated optical distortions during scanning (Nakamura et al., 2017).

An optical coupling box, housing a spectral wedge and a high-reflectivity mirror, is positioned beneath the sky scanner. The spectral wedge has a reflectivity of 0.95 and a transmittance of 0.05, allowing a frequency-stabilized He-Ne laser beam to be coupled into the system for calibration. A 250-mm-long baffle is installed below the optical coupling box to suppress stray light and limit the FoV to 2.5°.

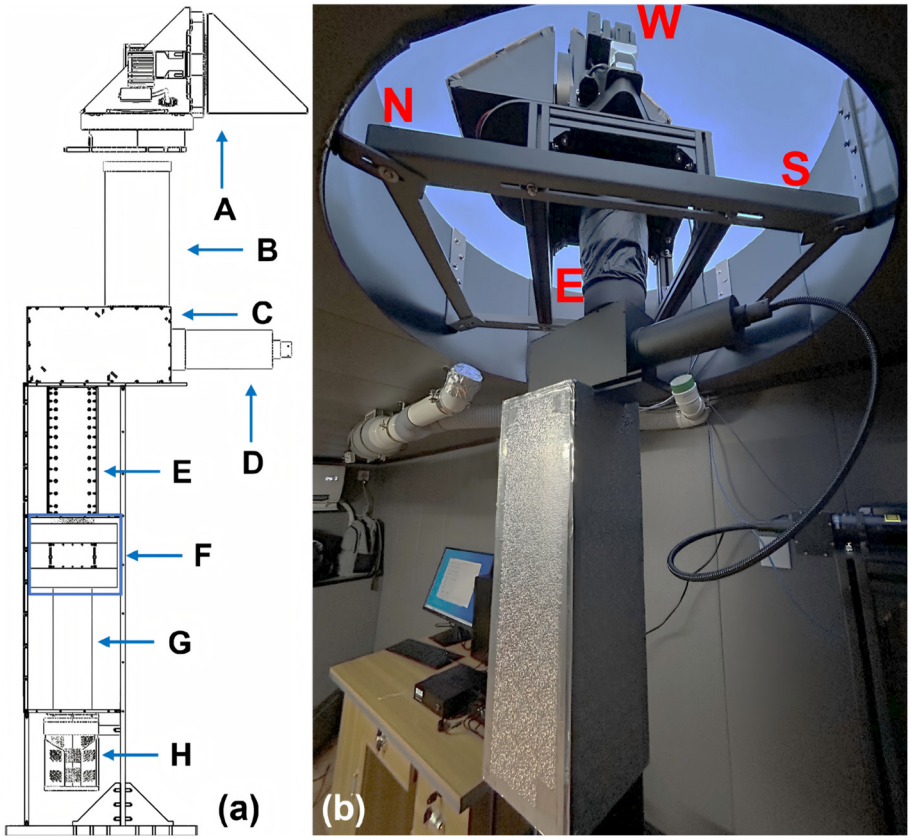

Figure 1. (a) Optical configuration and (b) photograph of the SEFPI system deployed at the observation station. The labeled components are: (A) sky scanner; (B) incident light tube; (C) optical coupling box for laser calibration and airglow observations; (D) laser scattering tube; (E) baffle; (F) interference chamber housing the bandpass filter and solid etalon; (G) focusing lens assembly; and (H) CCD detector.

The quasi-parallel beam from the baffle enters a sealed, temperature-controlled housing containing a bandpass interference filter and a solid etalon. The interference filter has a diameter of 75 mm, a central wavelength of 630.0 nm, and a bandwidth of 2.0 nm. The filtered atomic oxygen red-line emission then enters the solid etalon, where it produces concentric interference fringes. The solid etalon has a diameter of 70 mm and a thickness of 16 mm. The solid etalon is fabricated from fused silica, with a refractive index of 1.457, a reflectivity of 79%, and a surface flatness better than λ/100 over the clear aperture. Because the refractive index and physical thickness of the solid etalon are more sensitive to temperature variations, the spectral stability achievable for the typical etalon temperature stability of ±0.1 ℃ becomes a major technical challenge (Rees et al., 1982; Schmidt et al., 2025; Shiokawa et al., 2012; Wang et al., 2016; Wu et al., 2004). To address this issue, the solid etalon is housed in a temperature-controlled chamber maintained at 30 °C using an independently developed proportional-integral-derivative (PID) control system, with a target temperature stability of ±0.005 °C. During the 36 effective nighttime field observation periods, the measured etalon temperature showed a mean deviation of 0.0001 °C from the set point, with a standard deviation of 0.0026 °C (see Appendix, Figure A1).

An achromatic lens with a diameter of 100 mm and a focal length of 300 mm is used to image the interference pattern onto the focal plane of a cooled CCD detector. The detector is a PIXIS 1024B CCD camera with a 1024×1024 pixel array and a pixel size of 13 μm. It is cooled to -70 ℃ to reduce thermal noise during long-exposure observations. To increase the SNR, the CCD is operated in 2×2 binning mode, resulting in 512×512 pixel images.

Compared with conventional FPIs employing air-spaced etalons, the SEFPI is more compact and lightweight. The main components, excluding the CCD detector, are enclosed in an insulated aluminum housing to minimize the effects of ambient temperature fluctuations. Thermal insulation, not shown in panel (b) of Figure 1, is installed beneath the sky scanner to shield the instrument from direct sunlight during the daytime and limit heat transfer through the optical dome. Furthermore, a fan continuously circulates air across the dome surface to prevent nocturnal dew formation.

Table 1. System specifications of the SEFPI

Symbol	*Description*	*Specifications*
A	Sky scanner	Φ = 120 mm, Pointing accuracy of ±0.013°
B	Incident light tube	L = 200 mm, Φ = 110 mm, FoV = 2.5°
C	Optical coupling box	Optical spectral wedge (T/R = 0.05 : 0.95) Mirror (R≥97%@450-700 nm)
D	Laser scattering tube	L = 200 mm, Φ = 100 mm
E	Baffle	L = 250 mm, Φ = 75 mm, FoV = 2.5°
F	Interference chamber	Optical bandpass filter (Φ = 75 mm, FWHM = 2.0 nm, center wavelength of 630.0 nm) Solid etalon (Φ = 70 mm, d = 16 mm, n = 1.457, R = 0.78, surface flatness: λ/100) PID controller (Set temperature of 30°C with a stability better than ±0.005°C)
G	Focusing lens assembly	f = 300 mm, Φ = 100 mm
H	CCD detector	Princeton Instruments, PIXIS: 1024B_eXcelon 1024 × 1024 pixels, 13.312 mm × 13.312 mm

Figure 2 presents representative interferograms obtained by the SEFPI. Panel (a) shows the fringe pattern generated by a 632.8 nm frequency-stabilized He-Ne laser for system calibration, whereas panel (b) shows the interference pattern produced by the 630.0 nm atomic oxygen red-line nightglow emission. The integration times were 30 and 300 seconds for the laser calibration and red-line emission observations, respectively. Seven concentric interference rings are visible in both cases, providing sufficient spectral information for wind and temperature retrieval. The color bar on the right shows the 16-bit pixel grayscale intensity values of the CCD pixels.

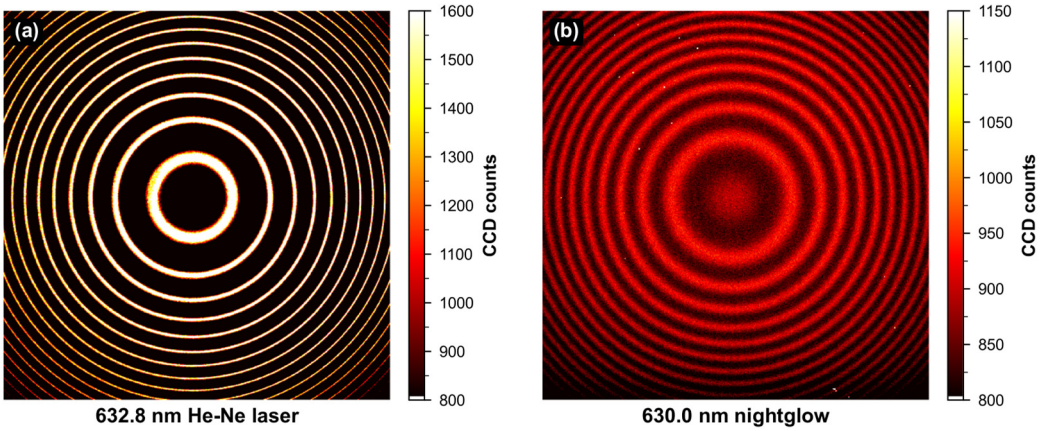

Figure 2. Interferograms observed by the SEFPI. (a) Calibration fringe pattern obtained using a 632.8 nm frequency-stabilized He-Ne laser with a 30 s exposure. (b) Nightglow fringe pattern of the 630.0 nm atomic oxygen red-line emission with a 300 s exposure.

3 Retrieval algorithm for wind and temperature from the interferogram

Various techniques have been developed to retrieve atmospheric winds and temperatures from FPI measurements. These include Gaussian fitting, Fourier series fitting, and nonlinear regression methods (Harding et al., 2014; Killeen and Hays, 1984; Makela et al., 2011; Shiokawa et al., 2003). Before retrieval, the raw images are preprocessed to improve the effective SNR and reduce computational complexity, following the procedure described by Makela et al. (2011). In this study, the nonlinear

regression method proposed by Harding et al. (2014) is adopted to retrieve atmospheric winds and temperatures from the measured interference fringes.

Unlike conventional FPIs equipped with air-spaced etalons, the SEFPI employs a solid fused-silica etalon. Therefore, the instrument function commonly used for air-spaced etalon FPIs cannot be applied directly to the SEFPI. To account for the optical properties of the solid etalon, the forward model is reformulated to explicitly incorporate the solid medium's refractive index and the corresponding optical path difference (OPD).

For a solid etalon, the OPD between the two transmitted beams after passing through the etalon can be expressed as,

$$OPD = 2nt\sqrt{1 - \left(\frac{sin^2(\theta(r))}{n^2}\right)} \tag{1}$$

Accordingly, the phase term in the instrument function can be written as,

$$\varphi = \frac{2\pi}{\lambda} \cdot OPD \tag{2}$$

Taking into account the actual imperfections of the optical system, the instrument function for the solid etalon is then formulated from the Airy function as,

$$\tilde{A}(r,\lambda) = \int_0^{r_m} b(s,r) \cdot \frac{I_0\left(1+I_1\left(\frac{s}{r_m}\right)+I_2\left(\frac{s}{r_m}\right)^2\right)}{1+\frac{4R}{(1-R)^2}\cdot\sin^2\left(\frac{\varphi}{2}\right)} ds \tag{3}$$

Here, λ denotes the nightglow emission wavelength, r represents the radial distance of the fringes, and s is a dummy variable corresponding to r. R, n, and t refer to the reflectivity, refractive index, and thickness of the solid etalon, respectively. $\theta(r)$ is the angle between the interference fringes and the optical axis, while r_m represents the maximum fringe radius. The parameters I_0, I_1, and I_2 denote the attenuation coefficients corresponding to average intensity, linear falloff and quadratic falloff, respectively. Finally, $b(s,r)$ is the point-spread function characterizing optical defects, as defined in Harding et al. (2014).

The system parameters are determined by minimizing the residuals between the model in Eq. (3) and the calibrated laser interference fringes using the Levenberg-Marquardt algorithm (Marquardt, 1963). The key technical parameters of the SEFPI are listed in Table 2, which were derived from ten He-Ne laser calibration interferograms at a wavelength of 632.8 nm. The measured reflectivity is 0.782 ± 0.001, and the measured etalon thickness is 15.999 mm ± 0.056 nm. Subsequently, the instrument function is convolved with the nightglow source spectrum to generate the modeled nightglow interference pattern.

$$Y(r) = \int_{\lambda_0 - N\cdot\delta\lambda_0/2}^{\lambda_0 + N\cdot\delta\lambda_0/2} \tilde{A}(r,\lambda)E(\lambda)\mathrm{d}\lambda + B_{ccd} \tag{4}$$

where λ_0 is the central wavelength of nightglow emission, $\delta\lambda_0$ represents the free spectral range (FSR), N is the number of FSRs spanned by the integration window, and B_{ccd} is the CCD detector bias. As the Airy function is periodic in wavelength with a period of FSR, the integration window is defined to span an integer number of FSRs. It ensures that the convolution accounts for complete interference orders without introducing partial orders at either boundary. The window must also be sufficiently wide to encompass the full Doppler-broadened emission line. As a result, N=4 is adopted to ensure adequate coverage of the line profile across the temperature range expected under both low- and high-solar-activity conditions.

In Eq. (4), $E(\lambda)$ is a Gaussian emission profile defined as,

$$E(\lambda) = B_{sky} + \frac{B_{line}}{\sqrt{2\pi}\cdot\Delta\lambda} \cdot exp\left(-\frac{1}{2}\frac{(\lambda-\lambda_c)^2}{\Delta\lambda^2}\right) \tag{5}$$

B_{sky} denotes the background sky emission intensity, and B_{line} represents the nightglow emission intensity. λ_c is the wavelength of the Doppler-shifted nightglow observed by the SEFPI.

$$\lambda_c = \lambda_0\left(1 + \frac{v_{los}}{c}\right) \tag{6}$$

$\Delta\lambda$ denotes the Doppler broadening of the emission line, which is related to the atmospheric temperature.

$$\Delta\lambda = \frac{\lambda_0}{c}\sqrt{\frac{kT}{m}} \quad (7)$$

In Eqs. (6) and (7), v_{los} represents the line-of-sight wind velocity, and T denotes the temperature. c, k, and m are the speed of light, the Boltzmann constant, and the mass of the emitting species, respectively. By combining Eqs. (1) -(7), the optimal values for line-of-sight wind and temperature are derived by minimizing the residuals between the modeled and observed nightglow interference fringes using a weighted least-squares method.

Table 2. Measured technical parameters of the SEFPI from laser calibration

Parameters	***Specifications***
Free Spectral Range (cm^{-1})	0.21448 ± 10^{-5}
Effective Finesse	12.3±0.1
Instrument Line Width (cm^{-1})	0.01744 ± 10^{-4}

4 Calibration and validation of SEFPI

To calibrate the SEFPI system and validate its wind-measurement performance, an acousto-optic frequency shifter (AOFS) was employed to generate controlled Doppler shifts, thereby simulating known wind velocities in the laboratory. In contrast to conventional retroreflective discs, this static device, modulated by radio-frequency signals, offers superior accuracy in wind-velocity simulation (Langille et al., 2013; Zhu et al., 2023). Figure 3 illustrates a schematic of the experimental setup used to measure Doppler shifts generated by the AOFS with the SEFPI. A frequency-stabilized He-Ne laser, operating at a wavelength of 632.8 nm, emits a beam that first traverses an optical isolator to suppress back reflections. The beam subsequently enters a beam splitter (BS), which divides it into two distinct optical paths. One path is directed to the SEFPI for system calibration after sequential reflection from mirrors M1 and M2. The second beam is focused by lens L1 and directed onto the AOFS crystal at an incident angle of 0.6°. Finally, the first-order diffracted beam from the AOFS passes through a pair of lenses (L2 and L3) and a diffuser, forming a uniform collimated beam that fills the SEFPI FoV. The simulated wind velocity V is related to the AOFS modulation frequency F by,

$$V = \frac{c\lambda_0 F}{\lambda_0 F + c\times10^3} \quad (8)$$

Here, λ_0 is the laser wavelength, c is the speed of light.

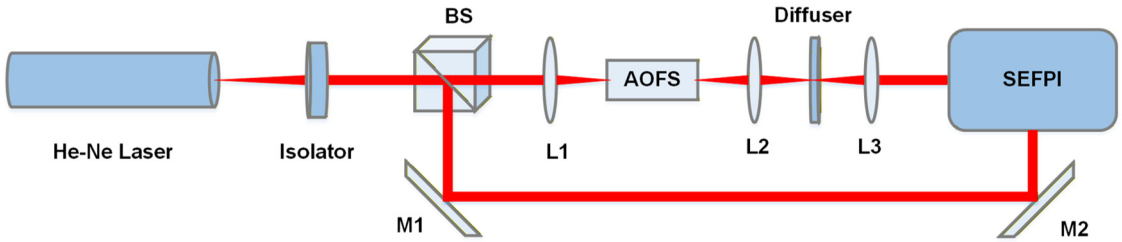

Figure 3. Schematic of the experimental setup for measuring Doppler shifts with the SEFPI using an AOFS. BS: beam splitter; L1-L3: focusing lenses; M1, M2: mirrors.

Initially, a dark frame image was acquired to correct subsequent CCD images during wind velocity measurements. For each simulated wind velocity, ten measurements were performed with an integration time of 5 seconds per measurement. A system calibration was performed before each wind velocity measurement. The AOFS driving frequency was varied from 100 to 200 MHz, corresponding to simulated wind velocities from −63.28 m/s to −126.56 m/s. The negative sign indicates the direction of incident light relative to the acoustic wave propagation in the crystal. The frequency was incremented by 4 MHz steps, resulting in 26 distinct settings across the full range. The AOFS has a frequency uncertainty of ±4 kHz, which is negligible compared with the laser's ±2 MHz frequency stability over one hour.

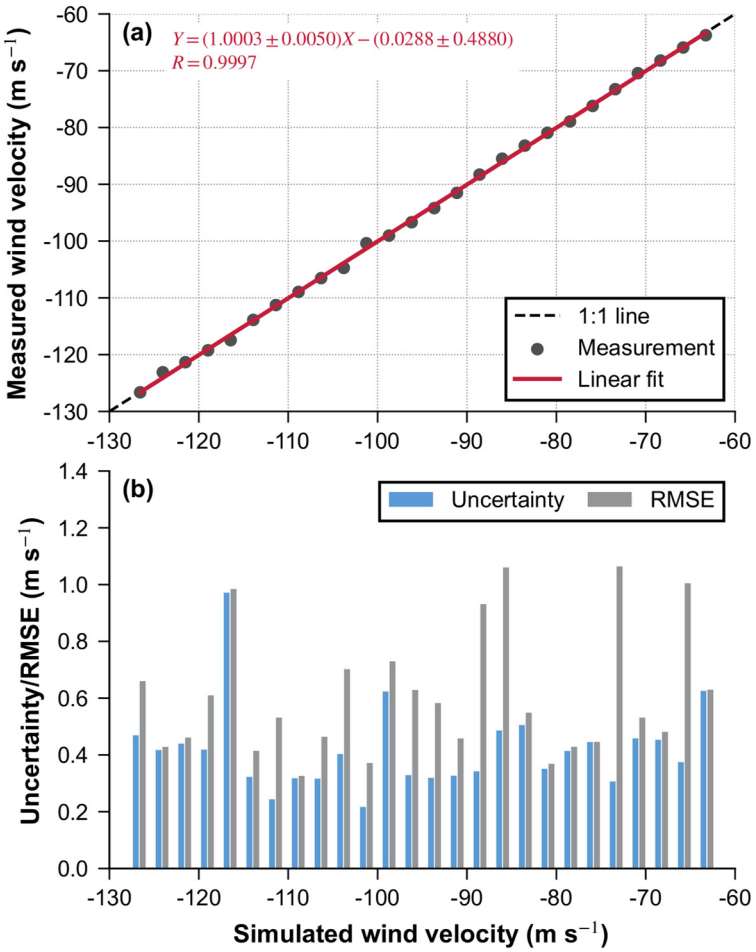

Figure 4. Experimental results of SEFPI wind measurements using Doppler shifts simulated by the AOFS. (a) Measured versus simulated wind velocities; (b) Measurement uncertainty and root mean square error (RMSE) derived from ten repeated measurements at each wind velocity.

Figure 4(a) compares the measured and simulated wind velocities, while Figure 4(b) presents the corresponding wind uncertainties (sky blue bars) and root mean square errors (RMSEs; gray bars) for each simulated wind velocity. The black dashed line represents the 1:1 reference line, corresponding to a perfect agreement between the measured and simulated wind velocities. Gray dots denote the average measured velocities from ten repeated measurements, and the red line represents the linear regression fit. The measured wind velocities exhibit excellent agreement with the simulated values. Linear regression yields a slope of 1.0003, an intercept of −0.0288 m/s, and a correlation coefficient (R) of 0.9997, demonstrating the SEFPI's high measurement accuracy in the laboratory. Furthermore, both the estimated uncertainty and RMSE for each simulated wind velocity remain below 1.1 m/s. Across 26 velocity points, the average values for wind uncertainty and RMSE are 0.42 m/s and 0.61 m/s, respectively.

5 Cross-comparison of field measurements from SEFPI

Field observations were conducted over a period of 54 days, from 14 March to 6 May 2024, at the Siziwang (SIZW) station (geog.: 41.5°N, 111.7°E; geom.: 36.9°N) in the north of China. To detect faint nocturnal atomic oxygen red-line emissions, the SEFPI integration time was set to 300 s per observation to ensure a sufficient SNR. The SEFPI observed sequentially at the zenith and at 45° elevation in the four cardinal directions, with a frequency-stabilized He-Ne laser exposure before each airglow exposure. A Dual-Channel Optical Interferometer (DCOI) had been deployed at this site as part of the Phase II network of the Chinese Meridian Project (CMP) (Wang et al., 2024). The DCOI, an Asymmetric Spatial Heterodyne Spectroscopy (ASHS) interferometer, derives neutral winds at altitudes of approximately 96 km and 250 km by simultaneously observing

atomic oxygen emissions at 557.7 nm and 630.0 nm. The instrument has a temporal resolution of 26 minutes; further technical details and measurement validations are available in Liu et al. (2025), Wei et al. (2020), and Zhu et al. (2023).

Given that neutral temperature measurement is not currently implemented in the DCOI systems, an FPI deployed at the Xinglong (XLO) station (geog.: 40.2°N, 117.4°E; geom.: 35.2°N) was selected for an independent intercomparison to evaluate the temperature measurement performance of the SEFPI (Wu et al., 2014; Yuan et al., 2010). The two sites are separated by approximately 502 km. Established during Phase I of the CMP, the XLO station was the first site within China's ground-based airglow observation network to be equipped with an FPI (Wang, 2010; Xu et al., 2021). This instrument, equipped with a fixed air-spaced etalon with a diameter of 100 mm, is designed as a three-channel system measuring OH emission at 892.0 nm (~87 km) and atomic oxygen emissions at 557.7 nm (~97 km) and 630.0 nm (~250 km) (Jiang et al., 2021; Wei et al., 2024). A complete observation cycle of the three airglow channels requires 31 minutes. Further details regarding this FPI instrument at the XLO station can be found in Li et al. (2021), Trondsen et al. (2019), and Vasilyev et al. (2017).

Before cross-comparison, the SEFPI, DCOI, and FPI observations were independently quality-controlled by removing measurements affected by cloud, precipitation, and moonlight contamination, as identified using cloud-sensor measurements and all-sky airglow images. In particular, the methodology described by Li et al. (2021) was adopted to identify and extract clear-sky observations from cloud sensor data. To mitigate moonlight contamination, a 37° exclusion threshold was applied to the angular separation between the Moon and the instrument's line-of-sight, based on the instrument's FoV and aperture. Following daily data screening, DCOI wind retrievals with uncertainties exceeding 75 m/s were excluded. This threshold was determined by the retrieval method and does not directly represent the actual wind measurement errors. For the SEFPI and XLO FPI, only measurements with quality flags of 0 and 1 were retained for subsequent analysis. At low and middle latitudes, thermospheric winds are commonly assumed to be spatially uniform across the four azimuthal viewing directions, while the mean vertical wind over an entire nighttime observing period is assumed to be zero (Harding et al., 2014; Makela et al., 2011; Tesema et al., 2017). Under these assumptions, the horizontal wind vector for each viewing direction was reconstructed from the line-of-sight wind using the method described by Vasilyev et al. (2017).

For the wind comparison, the northward and southward vector winds were first interpolated to common observation times and then averaged to obtain the representative meridional wind. The eastward and westward vector winds were processed similarly to derive the representative zonal wind. For the SEFPI and FPI temperature measurements, observations from the five viewing directions were first interpolated to a common reference time (i.e., the zenith observation time) and then averaged to obtain the representative temperature. To account for the different temporal sampling cadences of the three instruments, the DCOI and XLO FPI measurements were linearly interpolated to the corresponding SEFPI observation times before inter-instrument comparisons of both wind and temperature measurements.

During the 54-day campaign, the SEFPI was observed effectively on 36 nights, including 24 nights with valid simultaneous data from all three instruments (SEFPI, DCOI, and XLO FPI), 6 nights with valid SEFPI and DCOI data only, and 6 nights with valid SEFPI and FPI data only. Consequently, the SEFPI-DCOI and SEFPI-FPI intercomparisons each comprise 30 nights. Before analyzing the horizontal wind measurements of the SEFPI, the reliability of the retrieved wind zero point was evaluated using zenith observations. Analysis of quality-controlled zenith vertical wind measurements from the SEFPI over the 36 effective nights showed no appreciable systematic offset from zero (see Appendix, Figure A2).

5.1 Wind measurement comparison

Figures 5 and 6 show a daily comparison of horizontal winds at an altitude of 250 km, measured by three instruments from March to May 2024. Figure 5 compares the SEFPI and DCOI measurements, whereas Figure 6 compares the SEFPI and FPI measurements. Note that the error bars in the daily comparisons represent measurement uncertainty rather than the actual wind errors. Due to differences in interferometric configuration and wind retrieval methodology, the measurement uncertainties differ between the DCOI and SEFPI. Specifically, the SEFPI has a simpler optical configuration, and its wind retrieval is based

on direct fitting of the measured interference fringes. In contrast, the DCOI employs a more complex optical system and retrieves wind speed from phase variations in the interferograms using a windowed Fourier transform. Consequently, DCOI wind retrieval is more sensitive to the fringe contrast and SNR. Overall, the meridional and zonal wind components measured by the SEFPI show good agreement with those measured by both the DCOI at SIZW and the FPI at XLO. Nevertheless, quantitative discrepancies are observed, especially under low SNR conditions around local midnight, with the largest differences occasionally reaching ~59.00 m/s relative to the DCOI and ~53.39 m/s relative to the FPI.

Furthermore, all three instruments consistently captured the nocturnal temporal variations of thermospheric winds. Meridional winds typically flow southward, intensifying from dusk to midnight, peaking around midnight, and weakening towards dawn. Zonal winds generally reverse from eastward to westward between 14:00 and 20:00 UT. The timing of the zonal wind reversals is generally consistent within a given month but varies across months, consistent with the results reported by Jiang et al. (2018). Notably, the zonal winds observed on 26 April and 2 May, 2024, differed significantly from the typical daily variations. Specifically, following the reversal at 14:00 UT, the westward wind strengthened rapidly and peaked around 18:00 UT. This phenomenon was observed at both SIZW and XLO, with peak magnitudes of approximately 132.70 m/s (26 April) and 196.42 m/s (2 May).

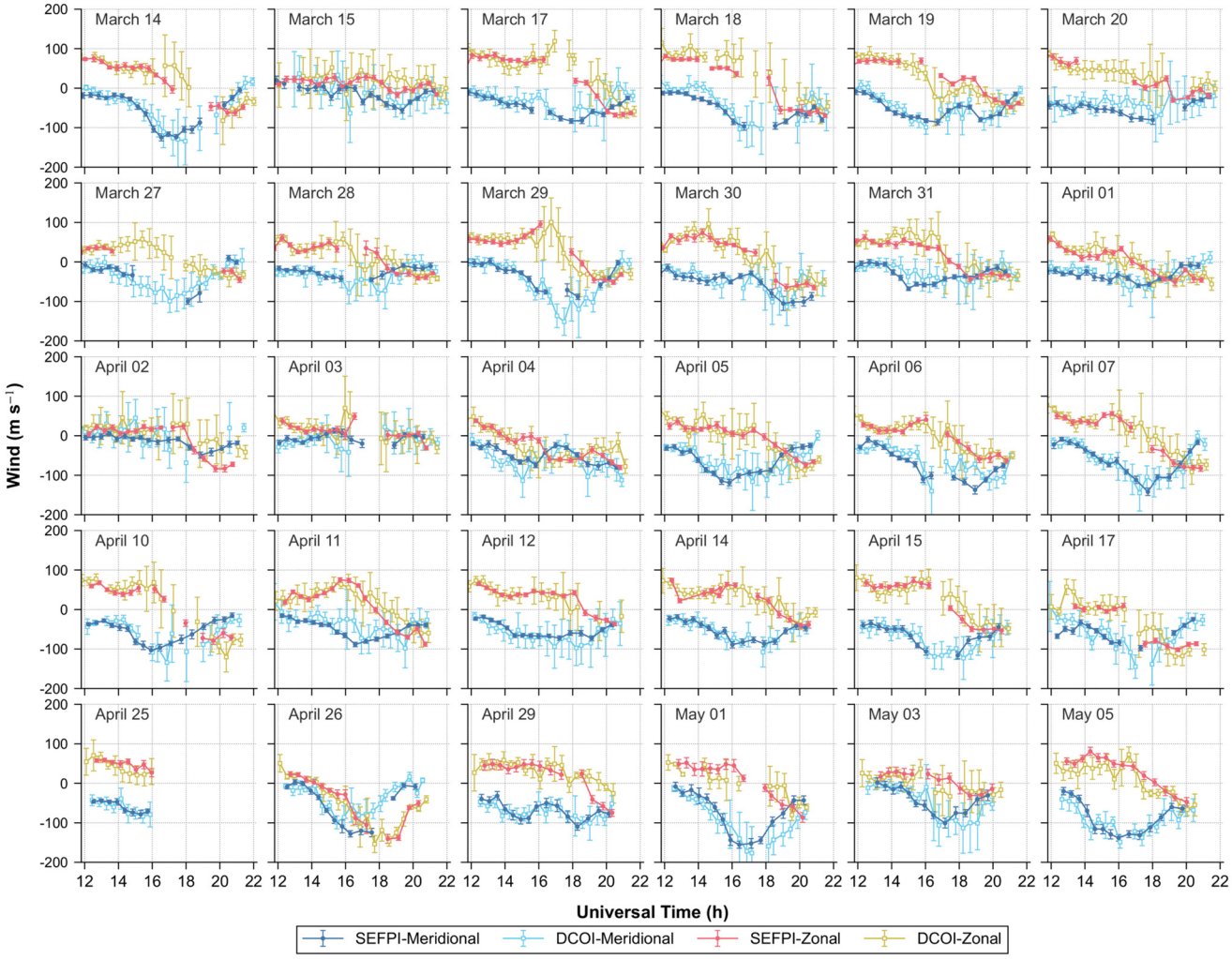

Figure 5. Daily comparison of wind measurements from the SEFPI and DCOI deployed at the SIZW station. Blue and pink solid circles denote the meridional and zonal winds measured by the SEFPI, respectively, while sky-blue and yellow hollow squares represent the corresponding DCOI measurements.

To quantify discrepancies between instruments, statistical comparisons were performed between the horizontal wind components measured by the SEFPI and those measured by the DCOI at SIZW and by the FPI at XLO. Figure 7 presents scatter plots comparing SEFPI wind measurements with DCOI and FPI measurements for the meridional (panels a and c) and zonal (panels b and d) components. At SIZW, the SEFPI and DCOI exhibit strong linear correlations, with correlation

coefficients of R=0.84 for the meridional component and R=0.90 for the zonal component. The fit slopes are 1.15 for the meridional component and 1.01 for the zonal component, indicating generally good consistency in wind variability between SEFPI and DCOI. This finding also shows that the DCOI wind measurements in magnitude are slightly higher than those from the SEFPI measurements. The mean differences (DCOI - SEFPI) are +1.35 m/s for the meridional component and +2.40 m/s for the zonal component, suggesting that the DCOI measurements are, on average, shifted toward more positive wind velocities relative to the SEFPI measurements. The standard deviations of the discrepancies are 20.49 m/s and 19.73 m/s, respectively. The zonal wind measurements exhibit better agreement than the meridional measurements. When the two horizontal wind components are considered together, the average of the mean difference was +1.88 m/s.

Similarly, comparisons between the SEFPI at SIZW and the FPI at XLO reveal a good agreement, with a higher correlation for the zonal component (R=0.93) than for the meridional component (R=0.85). The fit slopes are 0.88 for the meridional component and 0.89 for the zonal component, both below 1.0, indicating that the magnitude of the SEFPI winds is slightly larger than that of the FPI. The mean differences (FPI - SEFPI) are +4.92 m/s for the meridional component and +6.23 m/s for the zonal component, with a standard deviation of 17.66 m/s and 16.79 m/s, respectively. Therefore, the SEFPI measurements are, on average, shifted toward more negative wind velocities relative to the FPI measurements. Meanwhile, compared with the SEFPI-DCOI comparisons, the SEFPI-FPI comparisons exhibit larger mean differences.

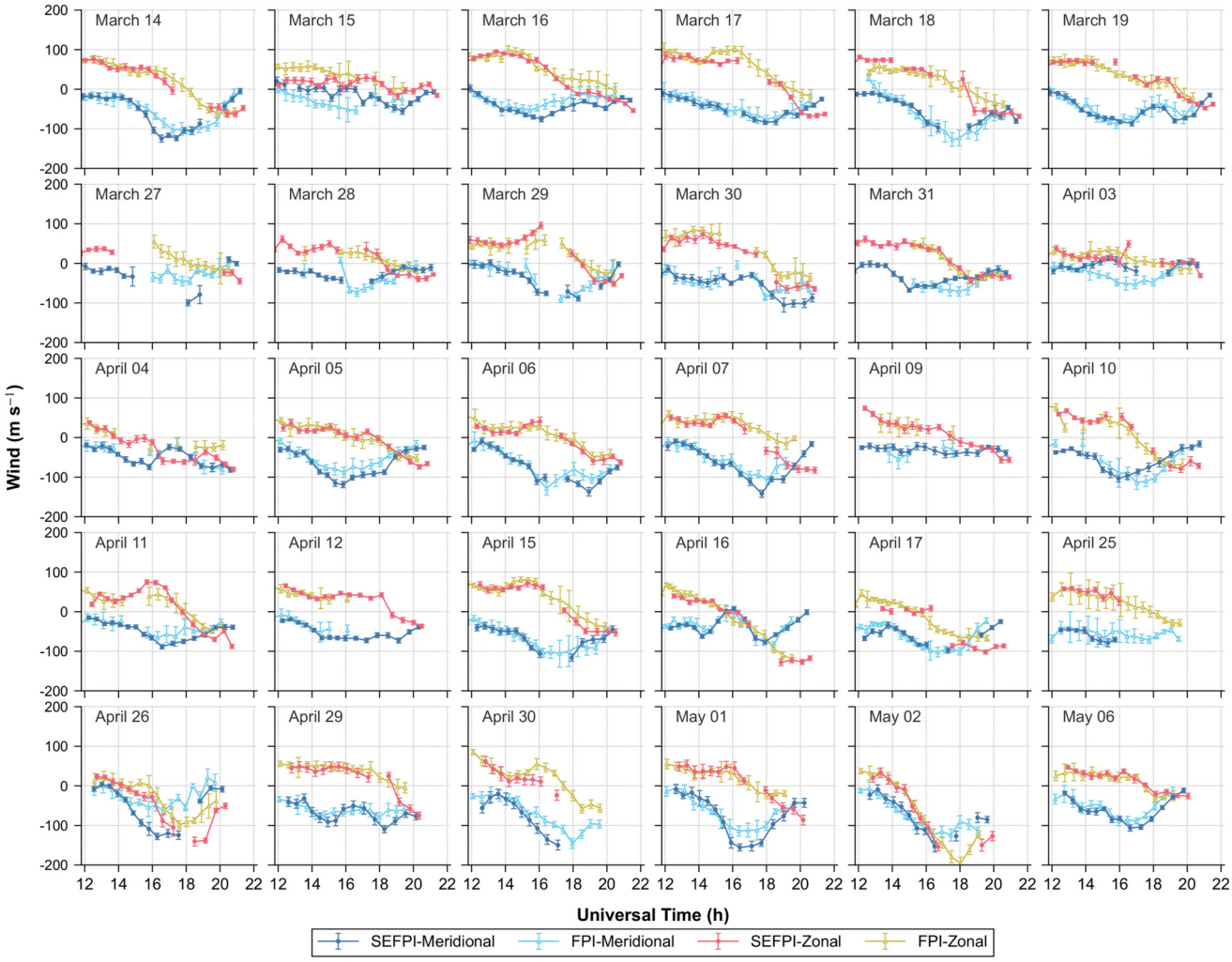

Figure 6. Daily comparison of wind measurements between the SEFPI at the SIZW station and the FPI at the XLO station, following the format of Figure 5. Blue and pink solid circles denote the meridional and zonal winds measured by the SEFPI, respectively, while sky-blue and yellow hollow triangles represent the corresponding XLO FPI measurements.

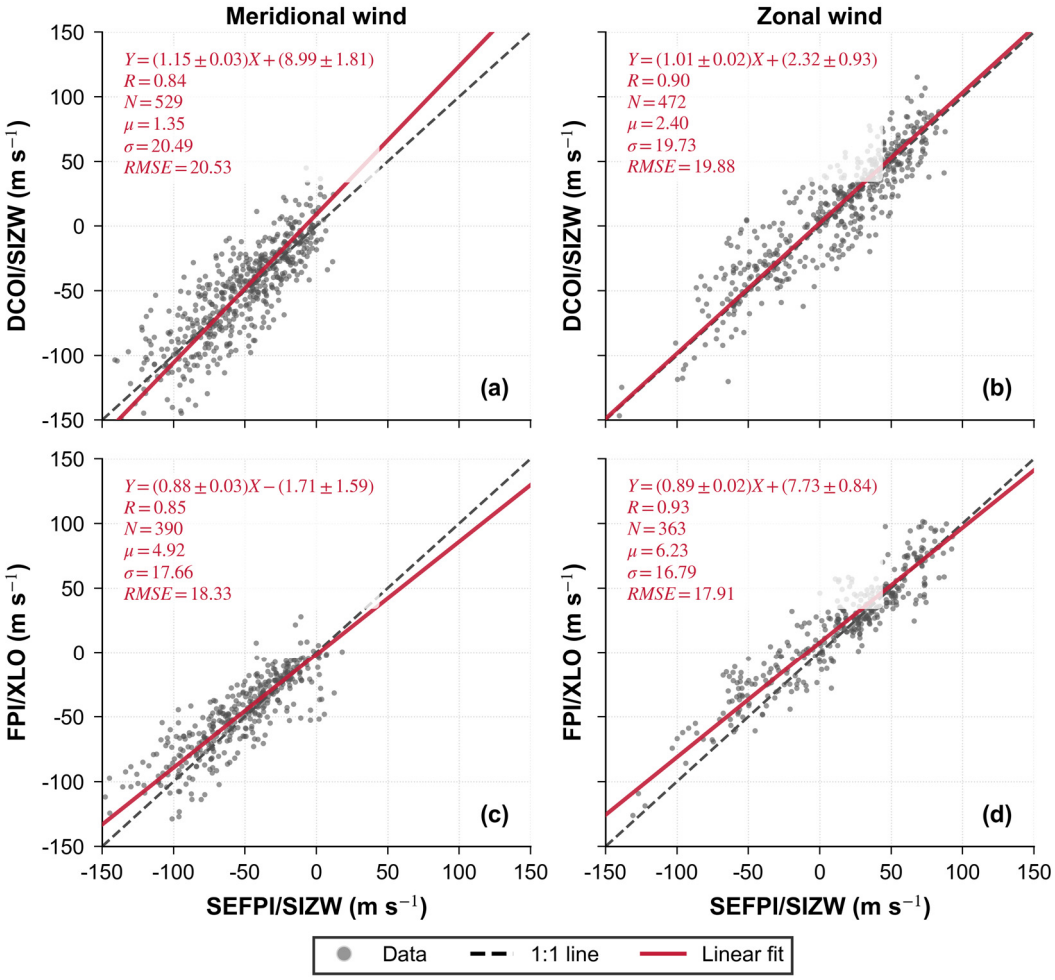

Figure 7. Statistical comparison of horizontal wind measurements. Panels (a) and (b) show the meridional and zonal wind comparisons between the SEFPI and DCOI, respectively, while panels (c) and (d) show the corresponding comparisons between the SEFPI and XLO FPI. In each subpanel, μ denotes the signed mean difference, σ is the standard deviation of the differences, N represents the number of paired samples, and RMSE shows the root mean square error.

5.2 Temperature measurement comparison

Figure 8 illustrates daily comparisons of thermospheric neutral temperatures measured independently by the SEFPI and FPI over multiple nights from March to May 2024. The plotted temperatures represent averages over five observation directions: the zenith and the four cardinal directions at an elevation angle of 45°. On most nights, the two instruments showed generally consistent temperature variations in both magnitude and temporal evolution. Temperature discrepancies between the two instruments were relatively small from dusk to midnight compared with the period from midnight to pre-dawn. The SEFPI and FPI temperature measurements showed close agreement during the first half of several nights, including March 14, 29, and 31, and April 6 and 10. However, the temperatures measured by the SEFPI were generally lower than those measured by the FPI, particularly during the pre-dawn hours. This discrepancy may be associated with the weaker 630.0 nm emission intensity during this period, which reduces the measurement SNR and increases the uncertainty of temperature retrieval (Meriwether et al., 2013). The maximum difference occasionally reaches 232.99 K. In addition, on nights such as April 4, 12, and 16, both the SEFPI and FPI measurements exhibited prominent Midnight Temperature Maxima (MTM) (Adachi et al., 2010; Chiang et al., 2018; Meriwether et al., 2013; Otsuka et al., 2003). Meanwhile, the equatorward meridional wind weakened rapidly but did not reverse direction, as shown in Figure 6.

To assess the potential influence of spatial variability from averaging the five viewing directions, the standard deviation of the temperatures measured in the five directions at each time point for both instruments was calculated. The error bars in Figure 8 represent these standard deviations and characterize the temperature dispersion among the five viewing directions. Except for the period around midnight, the directional temperature dispersion was consistently smaller than the mean temperature

difference between the two instruments. This finding indicates that, during most of the observation period, the temperature variability among the five viewing directions within each instrument was comparatively minimal relative to the inter-instrument temperature difference. Despite the approximately 502 km separation between the two instruments, which sample distinct atmospheric volumes, the modest directional dispersion suggests that aggregating the five viewing directions had a negligible effect on the overall temperature comparison during most observation periods. However, this averaging procedure may have smoothed out some local spatial and temporal variations.

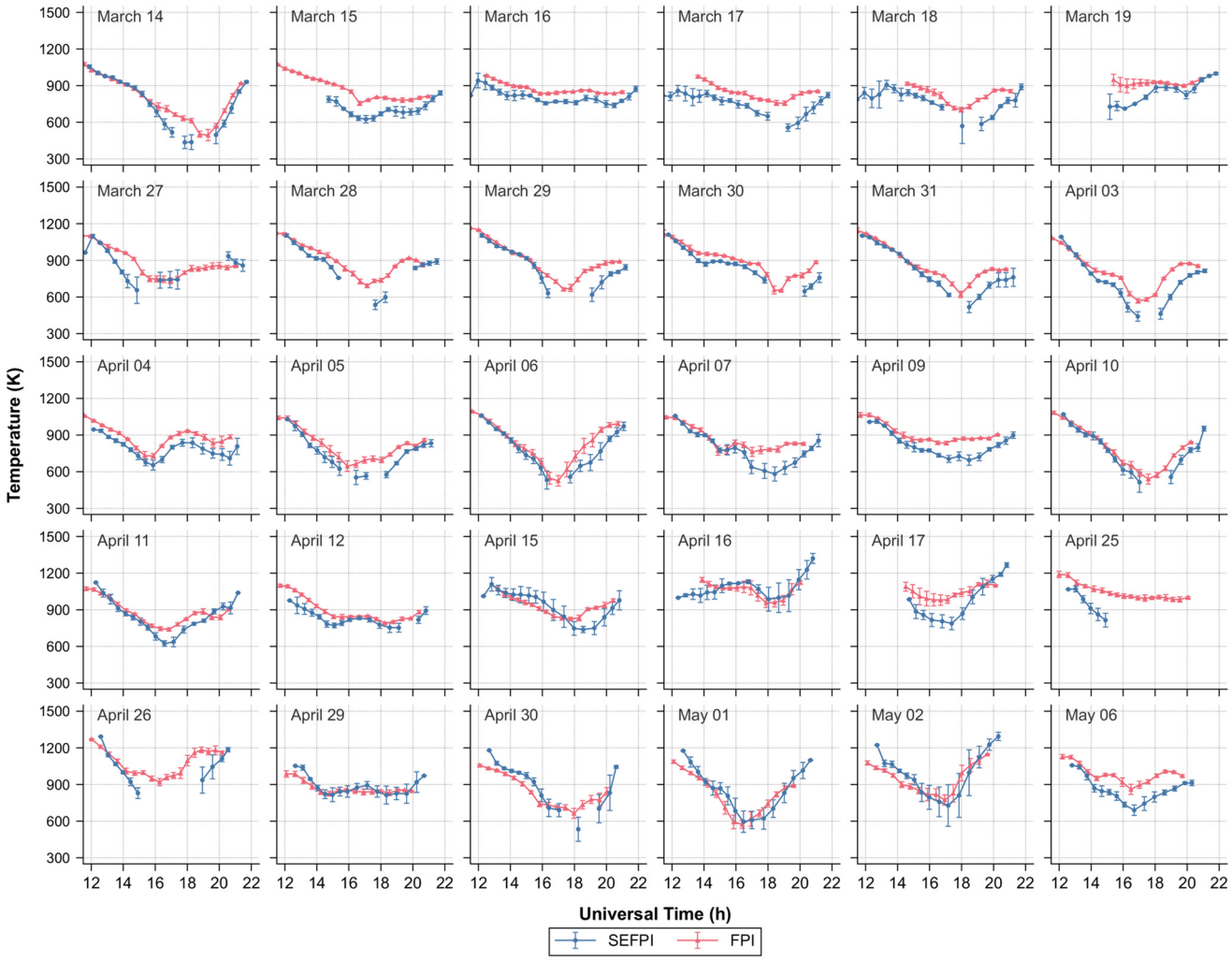

Figure 8. Daily comparison of temperature measurements between the SEFPI at the SIZW station and the FPI at the XLO station, following the format of Figure 6. Blue circles and pink triangles denote SEFPI and XLO FPI measurements, respectively. Each data point represents the average temperature from five observation directions. The error bars for each data point represent the dispersion of temperatures across the five directions before averaging them.

Scatter plots comparing SEFPI and FPI temperature measurements are shown in Figure 9. Analysis of 384 paired measurements yielded a correlation coefficient of R=0.86, indicating good agreement between the two instruments. The best-fit regression line has a slope of 0.77 and an intercept of 255.72 K, indicating a systematic bias between SEFPI and FPI temperature measurements. The mean temperature difference (FPI - SEFPI) was 62.38 K, with SEFPI generally yielding lower temperatures than FPI. The standard deviation of the temperature differences was 69.89 K. It is important to note that, due to the ~502 km spatial separation between the SIZW and XLO stations, the two instruments do not observe the same atmospheric volume and may experience different local thermospheric conditions. Therefore, these results should be interpreted as a temperature intercomparison and preliminary temperature validation demonstrating relative consistency, rather than a direct validation of the SEFPI's temperature accuracy.

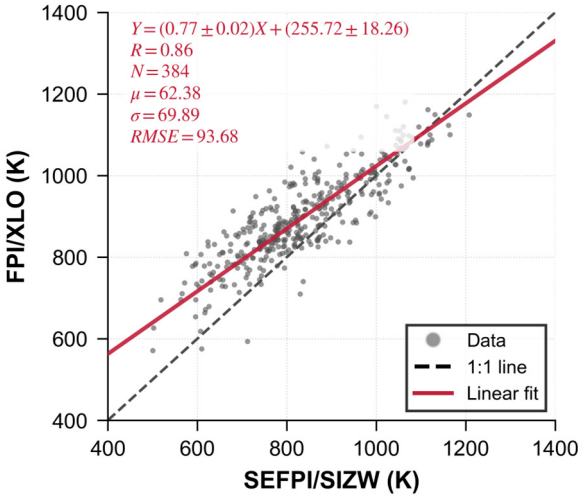

Figure 9. Statistical comparison of temperature measurements between the SEFPI at the SIZW station and the FPI at the XLO station, following the format of Figure 7. μ denotes the signed mean difference, σ is the standard deviation of the differences, N represents the number of paired samples, and RMSE shows the root mean square error.

6 Conclusion and discussion

This study presents a novel FPI employing a solid etalon that successfully measured atmospheric winds and temperatures at an altitude of approximately 250 km using the Doppler shift and spectral broadening of the atomic oxygen red line at 630.0 nm. Compared with conventional FPIs equipped with an air-spaced etalon, the SEFPI features a more compact, lightweight design. Significantly, it offers a potentially cost-effective solution to large-aperture etalons. Although this solution offers a substantial advancement in upper-atmospheric wind and temperature measurements, it also imposes more stringent requirements on the thermal stabilization of the solid etalon. The measurement capability of the SEFPI was validated in the laboratory using a newly developed high-precision setup for simulating controlled Doppler shifts. Field performance was further assessed during a 54-day deployment at the SIZW station by cross-comparing it with two independent passive optical instruments.

Laboratory validation demonstrated strong agreement between the measured and simulated wind velocities, yielding a linear regression slope of 1.0003, an intercept of −0.0288 m/s, and a correlation coefficient of 0.9997. These results confirm the high linearity and accuracy of the SEFPI system. Furthermore, wind measurement uncertainty and RMSE remained consistently below 1.1 m/s across the full simulated range, averaging 0.42 m/s and 0.61 m/s, respectively. These uncertainties may ascribe the expected contribution from the He-Ne laser frequency stability of ±2 MHz over one hour, corresponding to a wind velocity uncertainty of approximately 1.26 m/s.

To the best of our knowledge, this study presents the first simultaneous, co-located neutral-wind observations at an altitude of 250 km using a solid-etalon FPI and an ASHS interferometer. Coincident field measurements conducted from March to May 2024 demonstrate the SEFPI's reliable capability for thermospheric wind and temperature measurements. Overall, the SEFPI wind measurements exhibit good agreement with those from the co-located DCOI at SIZW and the FPI at XLO. The linear correlation coefficients exceeded 0.84 for both meridional and zonal wind components. Despite this agreement, notable discrepancies of up to ~59.00 m/s occasionally occurred under low-SNR conditions near local midnight, highlighting the sensitivity of these instruments to variability in nightglow intensity. Moreover, the SEFPI exhibited better agreement with the co-located DCOI than with the FPI at XLO. When both horizontal wind components are considered, the average of the mean differences (DCOI/FPI - SEFPI) is +1.88 m/s relative to the DCOI and +5.58 m/s relative to the FPI. The SEFPI temperature measurements also show good consistency with the FPI data, with a correlation coefficient of 0.86. The mean temperature difference was 62.38 K, with the SEFPI reporting slightly lower temperatures than the XLO FPI. On some nights, the

temperature differences reached a maximum of 232.99 K, with larger discrepancies generally occurring under weaker 630.0 nm emission conditions.

Several factors may contribute to the observed discrepancies in wind and temperature measurements among the SEFPI, DCOI, and FPI. First, differences in aperture size and optical throughput among the three instruments result in different SNRs for a given integration time. Second, due to differences in observational geometries, the FPI and DCOI sample airglow regions at slightly different locations and spatial volumes (Englert et al., 2012). For example, the SEFPI has a FoV of 2.5°, whereas the DCOI has a FoV of 9° (Liu et al., 2025; Wei et al., 2020). Consequently, at an altitude of 250 km, the corresponding DCOI sampling area is more than 12 times larger than that of the SEFPI. Third, the 502 km geographic separation between the SIZW and XLO stations leads to differences in the local thermospheric and lower-atmospheric conditions sampled by the two instruments. Consequently, this spatial separation limits the current comparison to a preliminary check of temperature consistency rather than a direct validation of temperature accuracy.

Additionally, distinct optical environments at each site may contribute to the observed discrepancies. Finally, spectral contamination from the OH Meinel emission at 629.79 nm is inevitable for FPI measurements of the 630.0 nm emission, particularly around midnight. For single-etalon FPI systems, significant systematic errors can arise when spectral contamination becomes appreciable; Kerr et al. (2023) reported that such errors can become significant when the OH emission brightness exceeds approximately 1/30 of the OI 630.0 nm emission intensity. Notably, the bandwidth of the bandpass filters used in the FPI (~0.8 nm) is significantly narrower than that of the SEFPI (~2.0 nm). Therefore, the SEFPI is more susceptible to OH contamination than the XLO FPI, particularly during periods of weak OI 630.0 nm emission. This difference in susceptibility may therefore contribute to the significant temperature discrepancies observed between the two instruments around midnight.

In conclusion, the SEFPI demonstrated robust measurement capabilities, achieving accurate wind measurements in laboratory validation and showing good agreement with coincident field observations. Given its compact design and cost-effectiveness, the SEFPI is well-suited for developing ground-based observational networks targeting the middle and upper atmosphere. The SEFPI therefore provides a promising approach for expanding observations of neutral winds and temperatures in the middle and upper atmosphere, although its solid etalon requires stringent thermal stabilization. Future work will focus on co-locating the SEFPI and the XLO FPI at the same site for direct measurement validation, including direction-by-direction temperature comparisons to characterize better spatial variability that the current directional averaging approach cannot fully resolve. In addition, a narrower-bandwidth interference filter will be employed in the SEFPI to investigate the observed temperature discrepancies further.

7 Appendix

A.1 Thermal stability of the solid etalon during field observations

The thermal stability of the solid etalon is an important factor affecting the long-term stability of the SEFPI, since variations in the etalon temperature can induce changes in its refractive index and physical thickness, thereby altering the instrumental spectral response. To evaluate the thermal stability under actual field operating conditions, we analyzed the solid etalon temperature recorded during the nighttime operation of the SEFPI. The dataset includes 36 effective nighttime observation periods. Because the SEFPI was operated only during nighttime airglow observations, the temperature records presented here correspond to the instrument's actual operating periods.

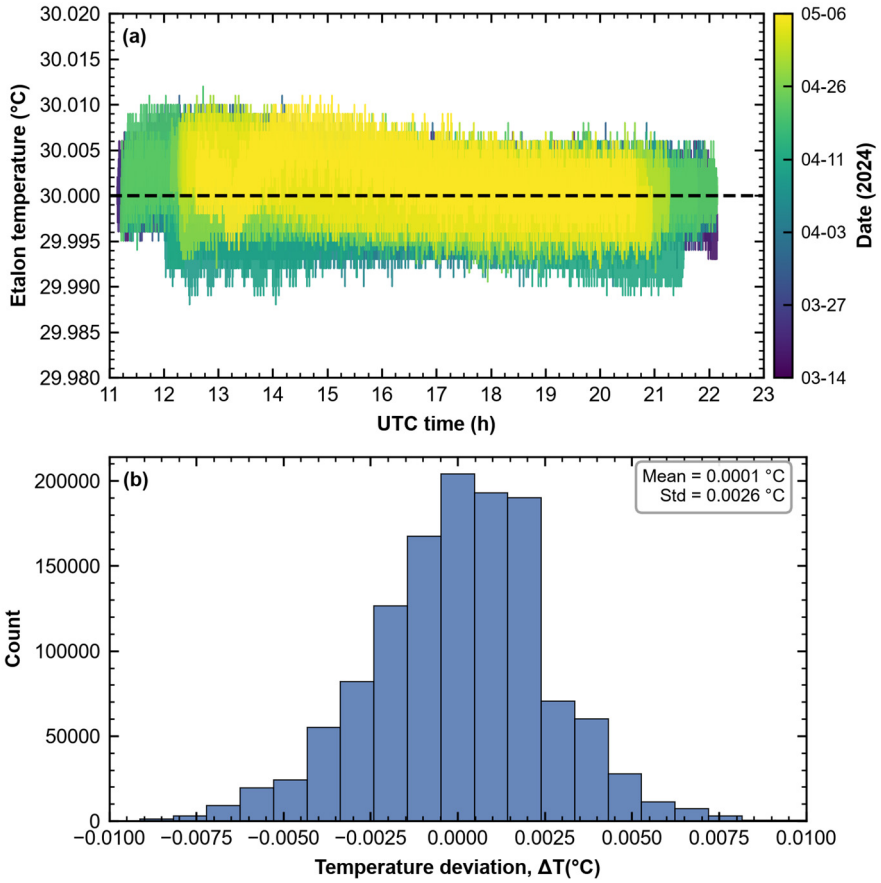

Figure A1. Thermal stability of the SEFPI solid etalon during field observations. (a) Measured solid-etalon temperature during 36 effective nighttime observation periods. The temperature control system sampled temperature at 1 measurement per second. The dashed line indicates the preset temperature of 30 °C, and the color scale represents the observation date. (b) Statistical distribution of the temperature deviation from the preset temperature. The mean deviation and standard deviation are 0.0001 °C and 0.0026 °C, respectively.

As shown in Figure A1(a), the measured etalon temperature remained closely centered on the preset temperature of 30 °C throughout the observation campaign, with no evident long-term drift. It is evident from Figure A1(b) that the corresponding temperature deviation is statistically distributed around zero. The mean deviation was 0.0001 °C, with a standard deviation of 0.0026 °C. These results demonstrate that the PID temperature-control system maintained the solid etalon with high thermal stability during the actual field observations.

A.2 Vertical winds for zenith direction during field observations

In the SEFPI field observations, a frequency-stabilized He-Ne laser exposure was acquired immediately before each airglow exposure. The laser measurement was used to characterize the instrumental response and determine the calibration parameters for the subsequent airglow retrieval. The wind and temperature were subsequently retrieved using a nonlinear regression method based on the airglow forward model, incorporating instrument system parameters calibrated from each laser measurement.

As an independent check of the wind zero-point, vertical winds for zenith observations obtained during the 36 effective nighttime field campaign were analyzed. A total of 404 quality-controlled zenith vertical wind measurements were retained. As shown in Figure A2(a), the retrieved vertical winds are distributed around zero throughout the observation period. The statistical distribution shown in Figure A2(b) gives a mean vertical wind of -0.19 m/s and a standard deviation of 5.64 m/s. The small magnitude of the mean value and the absence of an evident systematic displacement from zero indicate that there is no appreciable systematic wind offset.

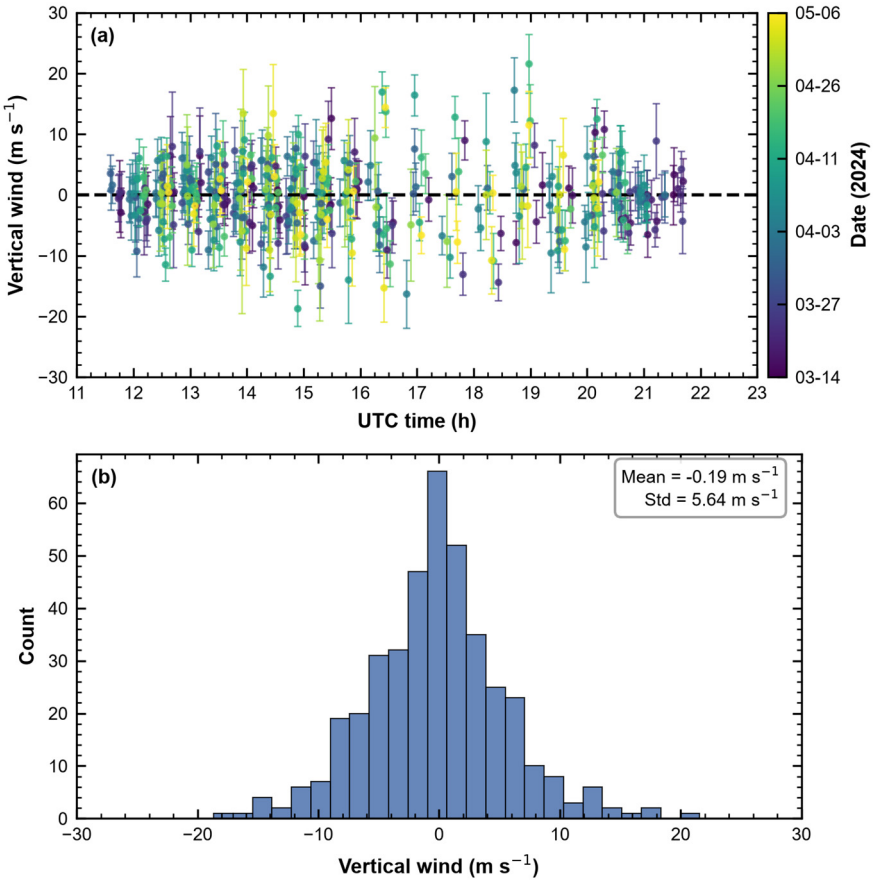

Figure A2. Zenith vertical wind measurements were obtained during 36 effective nighttime field observations. (a) Quality-controlled zenith vertical wind measurements. The error bars represent the corresponding wind-retrieval uncertainties, and the dashed line indicates zero vertical wind. Measurements are color-coded by observation date. (b) Statistical distribution of the zenith vertical wind measurements. The mean vertical wind is -0.19 m/s, with a standard deviation of 5.64 m/s.

Data availability

The DCOI data in this paper are available at the Chinese Meridian Project (https://dcstatus.meridianproject.ac.cn/). The SEFPI and the XLO FPI datasets for this study can be accessed via the website link provided by Wang (2026).

Author contributions

YZ conceptualized the study and contributed to the review and editing of the manuscript. TW was responsible for experimental design, instrument development and measurements, data processing, and preparation of the manuscript draft. HG and JX contributed to the review and editing of the manuscript. GZ performed the experimental validation. WL and WY carried out the instrument deployment and field measurements. QG and ZT conducted the etalon tests. All authors have read and agreed to the published version of the manuscript.

Competing interests

The corresponding author has declared that neither author has any competing interests.

Acknowledgments

All authors appreciate all the funding from the National Key R&D Program of China (2023YFB3905100), the Project of Stable Support for Youth Team in Basic Research Field, CAS (YSBR-018), the National Natural Science Foundation of China

(42174212, 62375285), the Science and Technology innovation Program of Hunan Province (2025RC1047), the Chinese Meridian Project, and the Specialized Research Fund for State Key Laboratory of Solar Activity and Space Weather. We acknowledge the use of atmospheric wind speed of Dual-Channel Optical Interferometer (DCOI) from the Chinese Meridian Project (DOI: 10.12176/01.05.00307-V01). We thank the staff of the Chinese Meridian Project (https://cstr.cn/31122.02.MSP) for their technical support and assistance in data collection and analysis. We sincerely thank all contributors to the development and deployment of the DCOI instruments. We would like to express our gratitude to the staff responsible for the operation and maintenance of the instruments at the SIZW and XLO stations. We are also grateful to the peer reviewers for their constructive comments and helpful suggestions, which greatly improved the manuscript.

Financial support

This work was supported by the National Key R&D Program of China (2023YFB3905100), the Project of Stable Support for Youth Team in Basic Research Field, CAS (YSBR-018), the National Natural Science Foundation of China (42174212, 62375285), the Technology Innovation Program of Hunan Province (2025RC1047), the Chinese Meridian Project, and the Specialized Research Fund for State Key Laboratory of Solar Activity and Space Weather.

References

Adachi, T., Yamaoka, M., Yamamoto, M., Otsuka, Y., Liu, H., Hsiao, C., Chen, A. B., and Hsu, R.: Midnight latitude-altitude distribution of 630 nm airglow in the Asian sector measured with FORMOSAT-2/ISUAL, J. Geophys. Res. Space Physics, 115, 2009JA015147, https://doi.org/10.1029/2009JA015147, 2010.

Anderson, C., Conde, M., Dyson, P., Davies, T., and Kosch, M. J.: Thermospheric winds and temperatures above Mawson, Antarctica, observed with an all-sky imaging, Fabry-Perot spectrometer, Ann. Geophys., 27, 2225–2235, https://doi.org/10.5194/angeo-27-2225-2009, 2009.

Aruliah, A. L., Griffin, E. M., Yiu, H.-C. I., McWhirter, I., and Charalambous, A.: SCANDI – an all-sky Doppler imager for studies of thermospheric spatial structure, Ann. Geophys., 28, 549–567, https://doi.org/10.5194/angeo-28-549-2010, 2010.

Biondi, M. A., Sipler, D. P., Zipf, M. E., and Baumgardner, J. L.: All-sky Doppler interferometer for thermospheric dynamics studies, Appl. Opt., 34, 1646–1654, https://doi.org/10.1364/AO.34.001646, 1995.

Chiang, C.-Y., Tam, S. W.-Y., and Chang, T.-F.: Variations of the 630.0 nm airglow emission with meridional neutral wind and neutral temperature around midnight, Ann. Geophys., 36, 1471–1481, https://doi.org/10.5194/angeo-36-1471-2018, 2018.

Conde, M. and Smith, R. W.: Phase compensation of a separation scanned, all-sky imaging Fabry–Perot spectrometer for auroral studies, Appl. Opt., 36, 5441–5450, https://doi.org/10.1364/AO.36.005441, 1997.

Dao, P., Farley, R., Tao, X., and Gardner, C.: Lidar Observations of the Temperature Profile Between 25 and 103 Km - Evidence of Strong Tidal Perturbation, Geophys. Res. Lett., 22, 2825–2828, https://doi.org/10.1029/95GL02950, 1995.

Dhadly, M., Sassi, F., Emmert, J., Drob, D., Conde, M., Wu, Q., Makela, J., Budzien, S., and Nicholas, A.: Neutral winds from mesosphere to thermosphere—past, present, and future outlook, Front. Astron. Space Sci., 9, 1050586, https://doi.org/10.3389/fspas.2022.1050586, 2023.

Englert, C. R., Harlander, J. M., Emmert, J. T., Babcock, D. D., and Roesler, F. L.: Initial ground-based thermospheric wind measurements using Doppler asymmetric spatial heterodyne spectroscopy (DASH), Opt. Express, 18, 27416–27430, https://doi.org/10.1364/OE.18.027416, 2010.

Englert, C. R., Harlander, J. M., Brown, C. M., Meriwether, J. W., Makela, J. J., Castelaz, M., Emmert, J. T., Drob, D. P., and Marr, K. D.: Coincident thermospheric wind measurements using ground-based Doppler Asymmetric Spatial Heterodyne (DASH) and Fabry–Perot Interferometer (FPI) instruments, J. Atmos. Sol. Terr. Phys., 86, 92–98, https://doi.org/10.1016/j.jastp.2012.07.002, 2012.

Fisher, G. M., Niciejewski, R. J., Killeen, T. L., Gault, W. A., Shepherd, G. G., Brown, S., and Wu, Q.: Twelve-hour tides in the winter northern polar mesosphere and lower thermosphere, J. Geophys. Res. Space Physics, 107, SIA 24-1-SIA 24-16, https://doi.org/10.1029/2001JA000294, 2002.

Gao, H., Xu, J., Ward, W., and Smith, A. K.: Temporal evolution of nightglow emission responses to SSW events observed by TIMED/SABER, J. Geophys. Res. Atmosphere, 116, n/a-n/a, https://doi.org/10.1029/2011JD015936, 2011.

Grawe, M. A., Chu, K. T., and Makela, J. J.: Measurement of atmospheric neutral wind and temperature from Fabry–Perot interferometer data using piloted deconvolution, Appl. Opt., 58, 3685, https://doi.org/10.1364/AO.58.003685, 2019.

Harding, B. J., Gehrels, T. W., and Makela, J. J.: Nonlinear regression method for estimating neutral wind and temperature from Fabry–Perot interferometer data, Appl. Opt., 53, 666–673, https://doi.org/10.1364/AO.53.000666, 2014.

Hernandez, G.: Measurement Of Thermospheric Temperatures And Winds By Remote Fabry-Perot Spectrometry, Opt. Eng., 19, 518–532, https://doi.org/10.1117/12.7972553, 1980.

Immel, T. J., Harding, B. J., Heelis, R. A., Maute, A., Forbes, J. M., England, S. L., Mende, S. B., Englert, C. R., Stoneback, R. A., Marr, K., Harlander, J. M., and Makela, J. J.: Regulation of ionospheric plasma velocities by thermospheric winds, Nat. Geosci., 14, 893–898, https://doi.org/10.1038/s41561-021-00848-4, 2021.

Jacka, F., Bower, A. R. D., Creighton, D. F., and Wilksch, P. A.: A large-aperture high-resolution Fabry-Perot spectrometer for airglow studies, J. Phys. E: Sci. Instrum., 13, 562–568, https://doi.org/10.1088/0022-3735/13/5/023, 1980.

Jia, Y., Chen, G., Xu, J., Yan, C., Zhang, S., Hu, L., Jia, W., Zhang, M., Gong, W., Xu, Y., Hu, P., and Yang, M.: Why Do Small-Scale Irregularities Migrate Beyond the Equatorial Plasma Bubble?, Geophys. Res. Lett., 52, e2024GL114399, https://doi.org/10.1029/2024GL114399, 2025.

Jiang, G., Xu, J., Wang, W., Yuan, W., Zhang, S., Yu, T., Zhang, X., Huang, C., Kerr, R. B., Noto, J., Li, J., Liu, W., and Li, Q.: A Comparison of Quiet Time Thermospheric Winds Between FPI Observations and Model Calculations, J. Geophys. Res. Space Physics, 123, 7789–7805, https://doi.org/10.1029/2018JA025424, 2018.

Jiang, G., Xiong, C., Stolle, C., Xu, J., Yuan, W., Makela, J. J., Harding, B. J., Kerr, R. B., March, G., and Siemes, C.: Comparison of Thermospheric Winds Measured by GOCE and Ground-Based FPIs at Low and Middle Latitudes, J. Geophys. Res. Space Physics, 126, e2020JA028182, https://doi.org/10.1029/2020JA028182, 2021.

Kerr, R. B., Kapali, S., Harding, B. J., Riccobono, J., Migliozzi, M. A., Souza, J. R., Mesquita, R., Dandenault, P., Wu, Q., Pimenta, A. A., Peres, L., and Silva, R.: Spectral Contamination of the 6300 Å Emission in Single-Etalon Fabry-Perot Interferometers, J. Geophys. Res. Space Physics, 128, e2023JA031601, https://doi.org/10.1029/2023JA031601, 2023.

Killeen, T. L. and Hays, P. B.: Doppler line profile analysis for a multichannel Fabry-Perot interferometer, Appl. Opt., 23, 612–620, https://doi.org/10.1364/AO.23.000612, 1984.

Kristoffersen, S. K., Ward, W. E., and Meek, C. E.: Wind comparisons between meteor radar and Doppler shifts in airglow emissions using field-widened Michelson interferometers, Atmos. Meas. Tech., 17, 3995–4014, https://doi.org/10.5194/amt-17-3995-2024, 2024.

Langille, J. A., Ward, W. E., Scott, A., and Arsenault, D. L.: Measurement of two-dimensional Doppler wind fields using a field widened Michelson interferometer, Appl. Opt., 52, 1617–1628, https://doi.org/10.1364/AO.52.001617, 2013.

Li, H., Zhang, J., Wang, W., Sun, L., Xu, J., Deng, X., Lan, A., Yan, J., Nishitani, N., and Wang, C.: Medium Scale Traveling Ionospheric Disturbances Observed by the SuperDARN Radars Located in the Asian Mid-Latitude, J. Geophys. Res. Space Physics, 130, e2025JA033978, https://doi.org/10.1029/2025JA033978, 2025.

Li, W., Chen, Y., Liu, L., Trondsen, T. S., Unick, C., Wyatt, D., Ning, B., Li, G., Huang, C., Yang, S., and Le, H.: Variations of Thermospheric Winds Observed by a Fabry–Perot Interferometer at Mohe, China, J. Geophys. Res. Space Physics, 126, e2020JA028655, https://doi.org/10.1029/2020JA028655, 2021.

Li, W., Liu, L., Chen, Y., Yang, Y., Han, T., Ding, F., Le, H., and Zhang, R.: Multi-Instruments Observation of Ionospheric-Thermospheric Dynamic Coupling Over Mohe (53.5°N, 122.3°E) During the April 2023 Geomagnetic Storm, J. Geophys. Res. Space Physics, 128, e2023JA032141, https://doi.org/10.1029/2023JA032141, 2023.

Liu, W. J., Zhu, Y. J., Xu, J. Y., Li, Q. Z., Yuan, W., Zhu, G. Y., Wang, T. C., Yang, G. T., Du, L. F., Liu, S. Y., and Li, F. Q.: Validation of Neutral Wind in the Mesopause Measured by a Dual-Channel Optical Interferometer (DCOI) Network of the Chinese Meridian Project, Space Weather, 23, e2025SW004468, https://doi.org/10.1029/2025SW004468, 2025.

Liu, X., Xu, J., Zhang, S., Zhou, Q., and Yuan, W.: Solar activity dependency of multiday oscillations in the nighttime thermospheric winds observed by Fabry-Perot interferometer, J. Geophys. Res. Space Physics, 120, 5871–5881, https://doi.org/10.1002/2015JA021375, 2015.

Makela, J. J., Meriwether, J. W., Lima, J. P., Miller, E. S., and Armstrong, S. J.: The Remote Equatorial Nighttime Observatory of Ionospheric Regions Project and the International Heliospherical Year, Earth, Moon and Planets, 104, 211–226, https://doi.org/10.1007/s11038-008-9289-0, 2009.

Makela, J. J., Meriwether, J. W., Huang, Y., and Sherwood, P. J.: Simulation and analysis of a multi-order imaging Fabry–Perot interferometer for the study of thermospheric winds and temperatures, Appl. Opt., 50, 4403–4416, https://doi.org/10.1364/AO.50.004403, 2011.

Makela, J. J., Harding, B. J., Meriwether, J. W., Mesquita, R., Sanders, S., Ridley, A. J., Castellez, M. W., Ciocca, M., Earle, G. D., Frissell, N. A., Hampton, D. L., Gerrard, A. J., Noto, J., and Martinis, C. R.: Storm time response of the midlatitude thermosphere: Observations from a network of Fabry-Perot interferometers, J. Geophys. Res. Space Physics, 119, 6758–6773, https://doi.org/10.1002/2014JA019832, 2014.

Makela, J. J., Baughman, M., Navarro, L. A., Harding, B. J., Englert, Christoph. R., Harlander, J. M., Marr, K. D., Benkhaldoun, Z., Kaab, M., and Immel, T. J.: Validation of ICON-MIGHTI Thermospheric Wind Observations: 1. Nighttime Red-Line Ground-Based Fabry-Perot Interferometers, J. Geophys. Res. Space Physics, 126, e2020JA028726, https://doi.org/10.1029/2020JA028726, 2021.

Marquardt, D. W.: An Algorithm for Least-Squares Estimation of Nonlinear Parameters, Journal of the Society for Industrial and Applied Mathematics, 11, 431–441, https://doi.org/10.1137/0111030, 1963.

Meriwether, J., Tepley, C., Price, S., Hays, P., and Cogger, L.: Remote Ground-Based Observations of Terrestrial Airglow Emissions and Thermospheric Dynamics at Calgary, Alberta, Canada, Opt. Eng., 22, 128–131, https://doi.org/10.1117/12.7973060, 1983.

Meriwether, J. W.: Studies of thermospheric dynamics with a Fabry–Perot interferometer network: A review, J. Atmos. Sol. Terr. Phys., 68, 1576–1589, https://doi.org/10.1016/j.jastp.2005.11.014, 2006.

Meriwether, J. W., Makela, J. J., Fisher, D. J., Buriti, R. A., Medeiros, A. F., Akmaev, R. A., Fuller-Rowell, T. J., and Wu, F.: Comparisons of thermospheric wind and temperature measurements in equatorial Brazil to Whole Atmosphere Model Predictions, J. Atmos. Sol. Terr. Phys., 103, 103–112, https://doi.org/10.1016/j.jastp.2013.04.002, 2013.

Nakajima, H., Okano, S., Fukunishi, H., and Ono, T.: Observations of thermospheric wind velocities and temperatures by the use of a Fabry–Perot Doppler imaging system at Syowa Station, Antarctica, Appl. Opt., 34, 8382–8395, https://doi.org/10.1364/AO.34.008382, 1995.

Nakamura, Y., Shiokawa, K., Otsuka, Y., Oyama, S., Nozawa, S., Komolmis, T., Komonjida, S., Neudegg, D., Yuile, C., Meriwether, J., Shinagawa, H., and Jin, H.: Measurement of thermospheric temperatures using OMTI Fabry–Perot interferometers with 70-mm etalon, Earth, Planets and Space, 69, 57, https://doi.org/10.1186/s40623-017-0643-1, 2017.

Okoh, D., Bounhir, A., Habarulema, J. B., Rabiu, B., Katamzi-Joseph, Z., Ojo, T., Wu, Q., and Makela, J. J.: Thermospheric Neutral Wind Measurements and Investigations across the African Region-A Review, Atmosphere, 13, 863, https://doi.org/10.3390/atmos13060863, 2022.

Otsuka, Y., Kadota, T., Shiokawa, K., Ogawa, T., Kawamura, S., Fukao, S., and Zhang, S. -R.: Optical and radio measurements of a 630-nm airglow enhancement over Japan on 9 September 1999, J. Geophys. Res. Space Physics, 108, 2002JA009594, https://doi.org/10.1029/2002JA009594, 2003.

Oyama, S., Vanhamäki, H., Cai, L., Shinbori, A., Hosokawa, K., Sakanoi, T., Shiokawa, K., Aikio, A., Virtanen, I. I., Ogawa, Y., Miyoshi, Y., Kurita, S., and Nishitani, N.: Thermospheric Wind Response to March 2023 Storm: Largest Wind Ever Observed With a Fabry-Perot Interferometer in Tromsø, Norway Since 2009, Space Weather, 22, e2023SW003728, https://doi.org/10.1029/2023SW003728, 2024.

Rees, D., Fuller-Rowell, T. J., Lyons, A., Killeen, T. L., and Hays, P. B.: Stable and rugged etalon for the Dynamics Explorer Fabry-Perot interferometer 1: Design and construction, Appl. Opt., 21, 3896–3902, https://doi.org/10.1364/AO.21.003896, 1982.

Saha, S. and Pallamraju, D.: Latitudinal variations in the nocturnal behaviour of OI 630 nm airglow emissions and their relationship with equatorial electrodynamics, J. Atmos. Sol. Terr. Phys., 241, 105965, https://doi.org/10.1016/j.jastp.2022.105965, 2022.

Schmidt, A. L., Meriwether, J. W., Cooper, M. B., Gerrard, A. J., Goodwin, L. V., Zhang, S.-R., and Ye, Y.: Detection of wave activity in measurements of thermospheric vertical winds and temperatures at subauroral latitudes, Front. Astron. Space Sci., 12, 1613164, https://doi.org/10.3389/fspas.2025.1613164, 2025.

Shiokawa, K., Kadota, T., Ejiri, M. K., Otsuka, Y., and Ogawa, T.: Three-channel imaging Fabry–Perot interferometer for measurement of mid-latitude airglow, Appl. Opt., 40, 4286–4296, https://doi.org/10.1364/AO.40.004286, 2001.

Shiokawa, K., Kadota, T., Otsuka, Y., Ogawa, T., Nakamura, T., and Fukao, S.: A two-channel Fabry-Perot interferometer with thermoelectric-cooled CCD detectors for neutral wind measurement in the upper atmosphere, Earth, Planets and Space, 55, 271–275, https://doi.org/10.1186/BF03351759, 2003.

Shiokawa, K., Otsuka, Y., Oyama, S., Nozawa, S., Satoh, M., Katoh, Y., Hamaguchi, Y., Yamamoto, Y., and Meriwether, J.: Development of low-cost sky-scanning Fabry-Perot interferometers for airglow and auroral studies, Earth, Planets and Space, 64, 1033–1046, https://doi.org/10.5047/eps.2012.05.004, 2012.

Sivjee, G. G., Hallinan, T. J., and Swenson, G. R.: Fabry-Perot-interferometer imaging system for thermospheric temperature and wind measurements, Appl. Opt., 19, 2206–2209, https://doi.org/10.1364/AO.19.002206, 1980.

Sun, L., Fang, X., Li, T., Yang, C., and Dou, X.: Design of a three-frequency Rayleigh lidar for simultaneous temperature and wind measurements, Opt. Express, 32, 25995, https://doi.org/10.1364/OE.527608, 2024.

Tesema, F., Mesquita, R., Meriwether, J., Damtie, B., Nigussie, M., Makela, J., Fisher, D., Harding, B., Yizengaw, E., and Sanders, S.: New results on equatorial thermospheric winds and temperatures from Ethiopia, Africa, Ann. Geophys., 35, 333–344, https://doi.org/10.5194/angeo-35-333-2017, 2017.

Trondsen, T. S., Unick, C., Wyatt, D., Meriwether, J. W., Chen, Y., and Li, W.: An Apochromatic Lens Based Fabry-Pérot Interferometer for Accurate Measurements of Lower Thermospheric Neutral Wind Velocity and Temperature, in: AGU Fall Meeting 2019, Abstract SA33B-3155, https://doi.org/https://keoscientific.com/wp-content/uploads/keosci-arinae-fpi-agu2019-poster.pdf, 2019.

Tsuda, T.: Characteristics of atmospheric gravity waves observed using the MU (Middle and Upper atmosphere) radar and GPS (Global Positioning System) radio occultation, Proc. Jpn. Acad. Ser. B-Phys. Biol. Sci., 90, 12–27, https://doi.org/10.2183/pjab.90.12, 2014.

Vasilyev, R. V., Artamonov, M. F., Beletsky, A. B., Zherebtsov, G. A., Medvedeva, I. V., Mikhalev, A. V., and Syrenova, T. E.: Registering Upper Atmosphere Parameters in East Siberia with Fabry–Perot Interferometer Keo Scientific “Arinae,” Solar-Terrestrial Physics, 3, 61–75, https://doi.org/10.12737/szf-33201707, 2017.

Wang, C.: New chains of space weather monitoring stations in China, Space Weather, 8, n/a-n/a, https://doi.org/10.1029/2010SW000603, 2010.

Wang, C., Xu, J., Chen, Z., Li, H., Feng, X., Huang, Z., and Wang, J.: China’s ground-based space environment monitoring network—Chinese meridian project (CMP), Space Weather, 22, e2024SW003972, https://doi.org/10.1029/2024SW003972, 2024.

Wang, H., Wang, Y., and Fu, J.: A Tiny Fabry-Perot Interferometer with Postpositional Filter for Measurement of the Thermospheric Wind, Acta Geophysica, 64, 2748–2760, https://doi.org/10.1515/acgeo-2016-0089, 2016.

Wang, T., Zhu, Y., Zhu, G., Xu, J., Ward, W. E., Liu, W., Wu, X., and Yuan, W.: Development and experimental validation of a signal-tracking Fabry-Perot interferometer for upper atmospheric wind measurements, Opt. Express, 33, 39724–39739, https://doi.org/10.1364/OE.570721, 2025.

Wang, T.: A Compact Fabry-Perot Interferometer with a Solid Etalon for Measuring Upper Atmospheric Wind and Temperature [Dataset], Zenodo, https://doi.org/10.5281/zenodo.23664978, 2026.

Wei, D., Zhu, Y., Liu, J., Gong, Q., Kaufmann, M., Olschewski, F., Knieling, P., Xu, J., Koppmann, R., and Riese, M.: Thermally stable monolithic Doppler asymmetric spatial heterodyne interferometer: optical design and laboratory performance, Opt. Express, 28, 19887–19900, https://doi.org/10.1364/OE.394101, 2020.

Wei, Y., Gu, S., Li, N., Qin, Y., Sun, R., Wang, D., Hu, G., Le, H., and Yuan, W.: Passive optical observation of mesosphere and thermosphere wind over three stations in China, J. Geophys. Res. Space Physics, 129, e2023JA032214, https://doi.org/10.1029/2023JA032214, 2024.

Wu, Q., Gablehouse, R. D., Solomon, S. C., Killeen, T. L., and She, C.-Y.: A new Fabry-Perot interferometer for upper atmosphere research, in: Fourth International Asia-Pacific Environmental Remote Sensing Symposium 2004: Remote Sensing of the Atmosphere, Ocean, Environment, and Space, 218–227, https://doi.org/10.1117/12.573084, 2004.

Wu, Q., Yuan, W., Xu, J., Huang, C., Zhang, X., Wang, J., and Li, T.: First U.S.-China joint ground-based Fabry-Perot interferometer observations of longitudinal variations in the thermospheric winds: US-China Joint FPI Observations, J. Geophys. Res. Space Physics, 119, 5755–5763, https://doi.org/10.1002/2014JA020089, 2014.

Wu, Q., Knipp, D., Liu, J., Wang, W., Varney, R., Gillies, R., Erickson, P., Greffen, M., Reimer, A., Häggström, I., Jee, G., and Kwak, Y.-S.: HIWIND Observation of Summer Season Polar Cap Thermospheric Winds, J. Geophys. Res. Space Physics, 124, 9270–9277, https://doi.org/10.1029/2019JA027258, 2019.

Xu, J., Li, Q., Sun, L., Liu, X., Yuan, W., Wang, W., Yue, J., Zhang, S., Liu, W., Jiang, G., Wu, K., Gao, H., and Lai, C.: The Ground-Based Airglow Imager Network in China: Recent Observational Results, in: Upper Atmosphere Dynamics and Energetics, American Geophysical Union, 365–394, https://doi.org/https://doi.org/10.1002/9781119815631.ch19, 2021.

Yang, C., Zhao, B., Jin, Y., Huang, C., Yao, X., and Wan, W.: Climatology of Nighttime Upper Thermospheric Winds From Fabry-Perot Interferometer 2011–2019 Measurements Over Kelan (38.7°N, 111.6°E), China: Local Time, Seasonal, Solar

Cycle, and Geomagnetic Activity Dependence, J. Geophys. Res. Space Physics, 125, e2020JA027892, https://doi.org/10.1029/2020JA027892, 2020.

Yi, W., Xue, X., Reid, I. M., Murphy, D. J., Hall, C. M., Tsutsumi, M., Ning, B., Li, G., Vincent, R. A., Chen, J., Wu, J., Chen, T., and Dou, X.: Climatology of the mesopause relative density using a global distribution of meteor radars, Atmos. Chem. Phys., 19, 7567–7581, https://doi.org/10.5194/acp-19-7567-2019, 2019.

Yuan, W., Xu, J., Ma, R., Wu, Q., Jiang, G., Gao, H., Liu, X., and Chen, S.: First observation of mesospheric and thermospheric winds by a Fabry-Perot interferometer in China, Chin. Sci. Bull., 55, 4046–4051, https://doi.org/10.1007/s11434-010-4192-2, 2010.

Yue, X., Wan, W., Ning, B., Jin, L., Ding, F., Zhao, B., Zeng, L., Ke, C., Deng, X., Wang, J., Hao, H., Zhang, N., Luo, J., Wang, Y., Li, M., Cai, Y., and Liu, F.: Development of the Sanya Incoherent Scatter Radar and Preliminary Results, J. Geophys. Res. Space Physics, 127, e2022JA030451, https://doi.org/10.1029/2022JA030451, 2022.

Zhang, N., Lei, J., Yue, X., Cai, Y., Wang, J., Wang, Y., Ding, F., Zhu, Y., and Ning, B.: Determination of the Mysterious O^+-O Collision Frequency Factor From the Sanya Incoherent Scatter Radar Measurements, Geophysical Research Letters, 52, e2025GL115928, https://doi.org/10.1029/2025GL115928, 2025.

Zhu, G., Zhu, Y., Kaufmann, M., Wang, T., Liu, W., and Xu, J.: An Efficient Calibration System of Optical Interferometer for Measuring Middle and Upper Atmospheric Wind, Remote Sensing, 15, 1898, https://doi.org/10.3390/rs15071898, 2023.